

SPACE-SUIT: An Artificial Intelligence based chromospheric feature extractor and classifier for SUIT

Pranava Seth^{1,2} · Vishal Upendran^{3,4} ·
Megha Anand^{2,5} · Janmejoy Sarkar^{2,6} ·
Soumya Roy² · Priyadarshan Chaki⁷ ·
Pratyay Chowdhury⁸ · Borishan Ghosh⁹ ·
Durgesh Tripathi²

© The author(s)

-
- ✉ Seth
pranavaseth@gmail.com
 - ✉ Upendran
vishal@lmsal.com
 - ✉ Anand
megha.anand@manipal.edu
 - ✉ Sarkar
janmejoy.sarkar@iucaa.in
 - ✉ Roy
soumya.roy@iucaa.in
 - ✉ Chaki
pdsnchaki@gmail.com
 - ✉ Chowdhury
pratyaychowdhury725@gmail.com
 - ✉ Ghosh
borishan.gh@gmail.com
 - ✉ Tripathi
durgesh@iucaa.in

- ¹ Thapar Institute of Engineering and Technology, Patiala, India - 147004
- ² Inter University Centre for Astronomy and Astrophysics, Pune, India - 411007
- ³ Bay Area Environmental Research Institute, NASA Research Park, Moffett Field, CA, USA - 94035
- ⁴ Lockheed Martin Solar and Astrophysics Laboratory, Palo Alto, CA, USA - 94304
- ⁵ Manipal Centre for Natural Sciences, Manipal Academy of Higher Education, Manipal, India - 576104

Abstract The Solar Ultraviolet Imaging Telescope (SUIT) onboard Aditya-L1 is an imager that observes the solar photosphere and chromosphere through observations in the wavelength range of 200-400 nm. A comprehensive understanding of the plasma and thermodynamic properties of chromospheric and photospheric morphological structures requires a large sample statistical study of these regions, necessitating the development of automatic feature detection methods. To this end, we develop the feature detection algorithm **SPACE-SUIT: Solar Phenomena Analysis and Classification using Enhanced vision techniques** for SUIT, to detect and classify the solar chromospheric features to be observed from SUIT’s Mg II k filter. Specifically, we target plage regions, sunspots, filaments, and off-limb structures for detection using this algorithm. SPACE uses You Only Look Once (YOLO), a neural network-based model to identify regions of interest. We train and validate SPACE using mock-SUIT images developed from Interface Region Imaging Spectrometer (IRIS) full-disk mosaic images in Mg II k line, while we also perform detection on Level-1 SUIT data. SPACE achieves a precision of ≈ 0.788 , recall of ≈ 0.863 and a MAP of ≈ 0.874 on the validation mock SUIT FITS dataset. Since our dataset is manually labeled, we perform ‘self-validation’ on the identified regions by defining statistical measures and Tamura features on the ground truth and predicted bounding boxes. We find the distributions of entropy, contrast, dissimilarity, and energy to show differences for the features in consideration. We find these differences to be captured qualitatively by the detected regions predicted by SPACE. Furthermore, we find these differences to also be qualitatively captured by the observed SUIT images, reflecting validation in the absence of a labeled ground truth. This work hence not only develops a chromospheric feature extractor, but it also demonstrates the effectiveness of statistical metrics and Tamura features in differentiating chromospheric features of interest, providing independent validation measures for any future detection and validation scheme.

1. Introduction

The lower solar atmosphere illustrates a complex interplay of fluid and magnetic processes that modulate the properties of the upper atmosphere and the heliosphere. Especially, the chromosphere is a complex region where magnetic and fluid effects play almost equal roles, manifesting several morphological structures like plage regions, filaments, sunspots, fibrils, and spicules. These structures are known to be coupled across the atmosphere, strongly influencing the dynamics

⁶ Department of Physics, Tezpur University, Napaam, Tezpur, Assam, India- 784028

⁷ Indian Association for the Cultivation of Science, Jadavpur, Kolkata, West Bengal, India - 700032

⁸ Hansraj College, University of Delhi, Delhi, India - 110007

⁹ Ramakrishna Mission Residential College, Narendrapur, Kolkata, Rajpur Sonarpur, West Bengal, India - 700103

across the atmosphere. Hence, understanding the properties and formation of these structures is crucial in understanding the dynamics of the solar atmosphere.

Aditya-L1 [38] is India's first space-based solar observatory. It was launched on 2 September 2023, and inserted into an L1-halo orbit around the Sun on 6 January 2024. The observatory has several remote-sensing and in-situ measurement instruments onboard, including spectrometers, plasma analyzers, and spectral imagers. The Solar Ultraviolet Imaging Telescope (SUIT) [39] is a spectral photometer onboard Aditya-L1, observing the solar atmosphere in the 2000-4000 Å wavelength range in eleven spectral bandpasses probing the photosphere and chromosphere. These spectral bandpasses contain 8 narrow bands and 3 broad bands, with a plate scale of 0.7"/px. SUIT produces routine full-disc images in the NB3 filter, centered around the Mg II k line at ≈ 2796 Å. Extensive statistical studies of chromospheric features of interest demand automated feature detection and extraction methods operating on the NB3 passband. Hence, it is hence imperative to develop algorithms to detect chromospheric morphological features observed by SUIT, which will be made available to the community as a Level 2+ data product by the team.

Feature extraction, detection and segmentation are well-known problems in heliophysics, solved either using empirical or learning-based methods. For instance, sunspot identification has been a classic problem, with several efforts on automating the process [12, 15, 29, 48, 8, 41]. Similarly, automated filament detection is a classic problem, with several efforts in the past [33, 47, 2, 25, 16, 14], along with detection of plages [5, 4]. Most of these systems are demonstrated with either (i). A specific feature of interest, or (ii). A specific telescope/set of telescopes of interest. More precisely, each telescope in consideration has observed the Sun in different bandpasses, has different instrument characteristics, and hence would have different features of interest.

In this article, we describe the development of a feature detection system for SUIT, called **SPACE: Solar Phenomena Analysis and Classification using Enhanced vision techniques**. This is a supervised deep learning algorithm and is based on the visual detection model YOLO [45]. With **SPACE**, we are specifically interested in the following features from SUIT: (i). Plages, (ii). Filaments, (iii). Sunspots, and (iv). Off-limb structures, and deploy the algorithm for the NB3 passband of SUIT. In general, the evaluation of proposed feature identification algorithms critically depends on a well-defined ground truth.

In this work, we propose a framework using statistical measures and Tamura features to evaluate both the ground truth and predictions, presenting measures that may be used for auto-validation of feature detection methods. Previous studies have demonstrated the utility of statistical moments, such as skewness and kurtosis, in effectively analyzing solar flare activities and revealing pre-flare signatures [43]. Similarly, texture-based features, including Tamura directionality and contrast, which have been widely utilized for solar image analysis, have shown significant potential, particularly for feature recognition and tracking [3, 36, 35, 21, 1, 22]. We train and evaluate **SPACE** on mock-SUIT images, and perform a zero-shot prediction on the SUIT observations.

In the following sections, we first describe the development of mock SUIT images in §. 2.1, and describe the data processing in §. 2.2. In §. 3, we present

the automatic detection algorithm. In §. 4, we present a self-validation scheme using statistical and Tamura information, while in §. 5, we also present all the results and a definition of the compiled catalog.

2. Dataset preparation

2.1. Mock SUII image generation

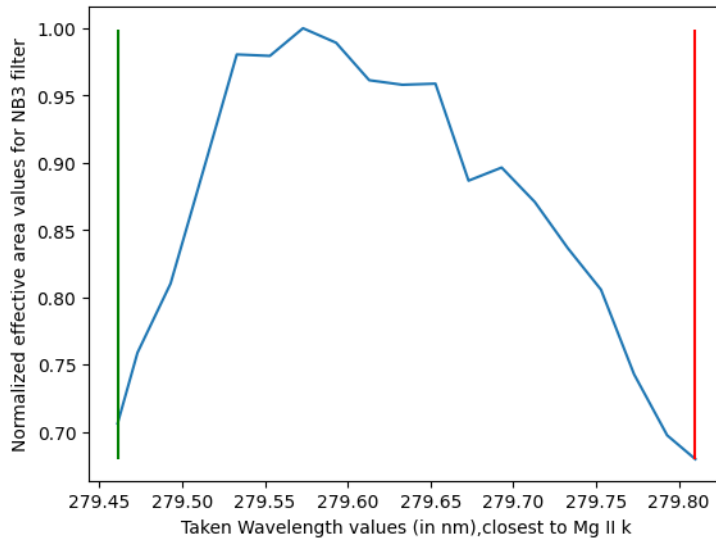


Figure 1. Effective Area of NB3 filter of SUII normalized by its peak, coinciding with the wavelength range IRIS Mg II k mosaics. The green and red vertical lines specify lower and higher wavelength limits recorded by IRIS, respectively.

SPACE is a supervised learning algorithm, that needs pairs of input images, bounding boxes. These input images, on deployment of the workflow, would be the SUII images. As of this manuscript, SUII has not generated enough data for developing a supervised detection model. Hence, we develop a catalogue of ‘mock’ SUII images using data recorded by the Interface Region Imaging Spectrograph (IRIS) [13].

IRIS contains a spectrograph and a slit-jaw imager, and performs observations in near ultraviolet (NUV) and far ultraviolet (FUV) regimes. The spectroscopy is performed in three windows, one in near ultraviolet (NUV) from 2782.7 to 2851.1 Å, and two in the far ultraviolet (FUV), from 1332 to 1358 Å (FUV 1), and from 1389 to 1407 Å (FUV 2). IRIS periodically takes a full-disk mosaic in the 6 spectral windows surrounding the strongest spectral lines, by combining rasters taken at different pointings covering the full disc. The observation program covers ≈ 185 pointings across ≈ 18 hours, by constructing a 64-step raster

with step size of ≈ 2 arcsec, at an exposure time of 1-2 seconds, with a spectral resolution of 0.035 \AA . These rasters are available on the IRIS website ¹.

We use ≈ 10 years (30-09-2013 – 23-07-2023) of Mg II k full-disc mosaics in this work to generate mock-SUIT images in the NB3 passband with a filter combination of CF1, which has a central wavelength of 2796 \AA . To construct mock SUIT images, we perform the following steps:

1. Normalize the SUIT effective area to the maximum value. The normalized effective area, along with the wavelength range of IRIS observations is shown in Fig. 1.
2. This normalized effective area is multiplied with IRIS mosaic pixel values, and summed across all wavelength bins. Two examples of wavelength-summed IRIS Mg II k mosaics are shown in Fig. 2. These two images will serve as our test bed for demonstrating various cleaning operations and mock-SUIT image generation performed through this section.

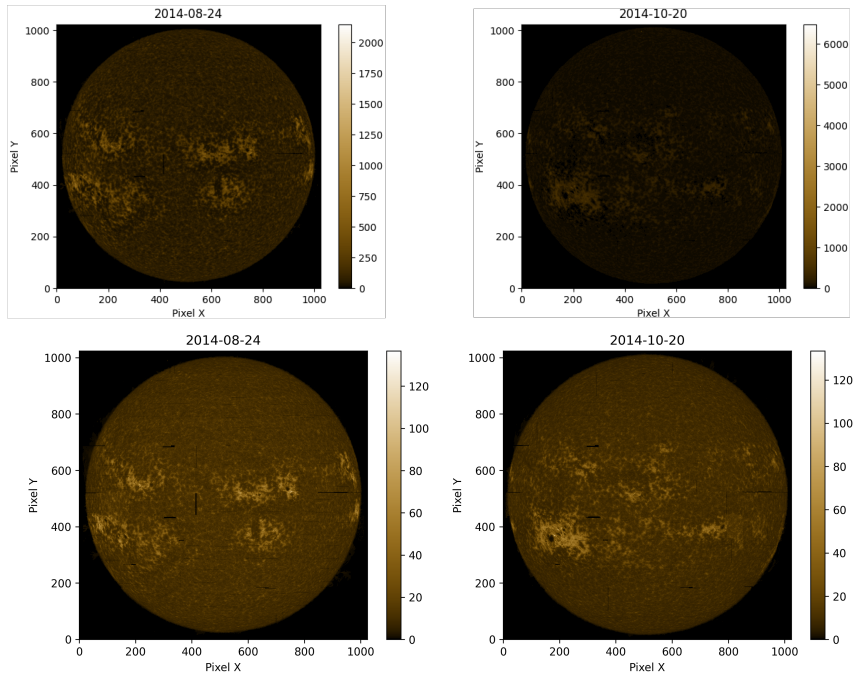


Figure 2. IRIS mosaic pixel values at the central wavelength of 2796 \AA (top row). The same IRIS mosaics folded with the normalized NB3 effective area (bottom row).

3. All IRIS mosaics are affected by spikes due to cosmic rays, which are not removed by default. To remove such cosmic ray spikes, we used a median filter [18] with a kernel size of 5 pixels. The median-smoothed images are shown in Fig. 3

¹https://iris.lmsal.com/mosaic_allin1.html

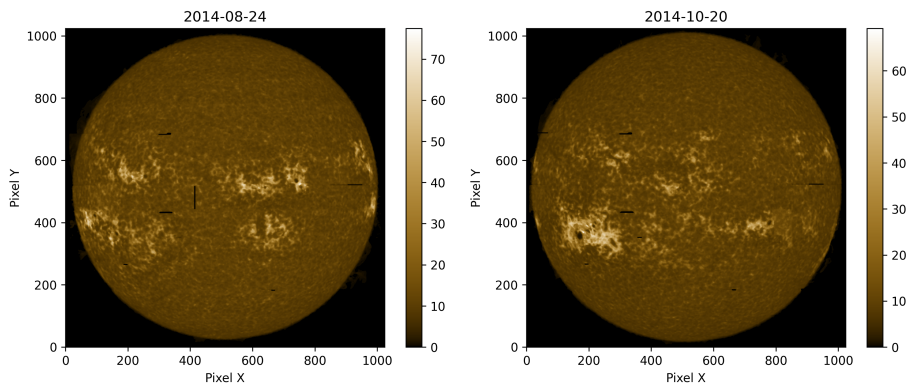


Figure 3. The working samples from bottom row of Fig. 2 after removing cosmic rays, using a 5×5 median filter.

4. The IRIS mosaics have dark horizontal or vertical lines due to mosaic stitching. To remove these artifacts, we performed a combination of Binary Inverse and Otsu thresholding [28] to identify the dark pixels, which we treated as background. Binary Threshold tends to separate foreground and background with a single value, while Otsu’s threshold algorithm seeks to find the intensity value that maximally separates intensity distribution into two Gaussians. The intensity masks are displayed in the left columns of Fig. 4. We use these masks to perform inpainting [23] using the Navier Stokes function from OpenCV. At its core, this method the lines of constant intensity (i.e. Isophotes) constantly from the exterior into the area that has to be painted. It considers the image intensity as a 2-D incompressible flow’s “stream function”. The Laplacian of the image intensity represents the fluid’s vorticity, which is carried into the area that has to be painted by a vector field that is determined by the stream function. The resulting algorithm’s goal is to match gradient vectors at the edge of the inpainting zone while maintaining isophotes. A detailed explanation of the method is provided in [6]. The data obtained after inpainting are shown in the bottom row of Fig. 4.
5. The angular resolution of IRIS mosaics is $0.33''/\text{px}$ along the y-axis and $1.99''/\text{px}$ along the x-axis. We interpolate the image to ensure that the angular resolution of both axes was equal to $0.33''/\text{px}$. We then convolved the interpolated image with the measured Point Spread Function (PSF) values corresponding to SUIT NB3, as shown in Fig. 5. We then degrade the images to $0.7''/\text{px}$ and bin them to 1024×1024 spatial resolution to obtain the final image, as shown in Fig. 6 .

2.2. Data processing

We manually label the prepared dataset using Roboflow ² by identifying the four features of interest: plages, filaments, sunspots, and off-limb structures.

²<https://roboflow.com/>

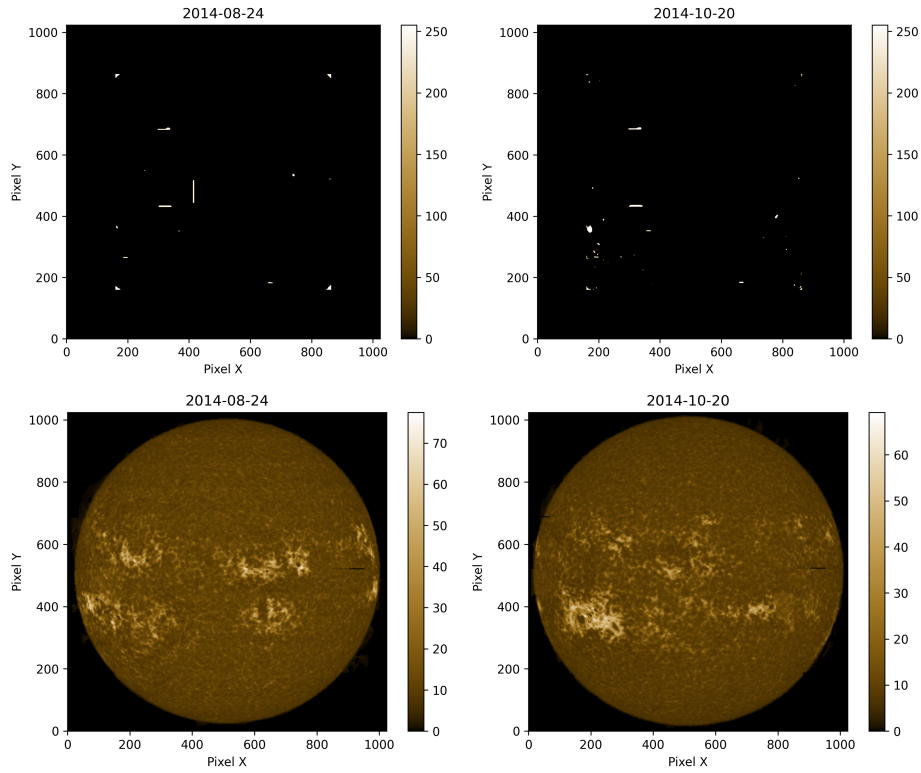


Figure 4. Masks obtained by applying the Inverse Thresholding on the working samples from Fig. 3 are displayed in the top row. The corresponding inpainted images are displayed in the bottom row.

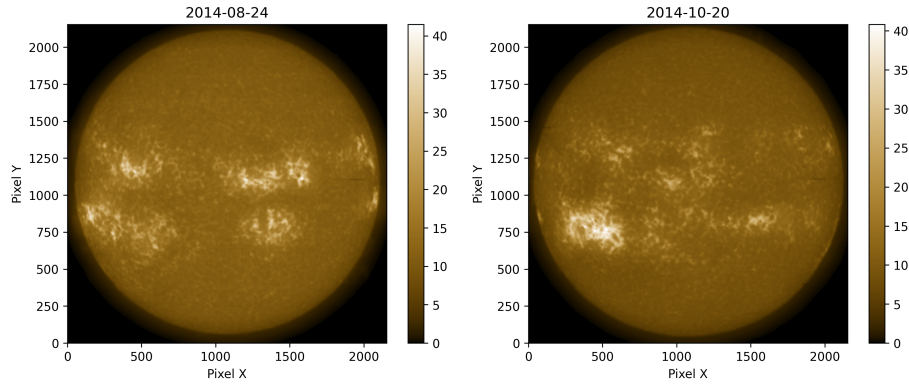


Figure 5. The inpainted image from Fig. 4 after convolving with the SUI3 NB3 PSF and rebinned to $0.7''$ per pixel.

The annotation is performed in the Oriented Bounding Box format (OBB) [20]³. In this labeling format, each box is defined by the coordinates at the four vertices

³<https://docs.ultralytics.com/datasets/obb/>

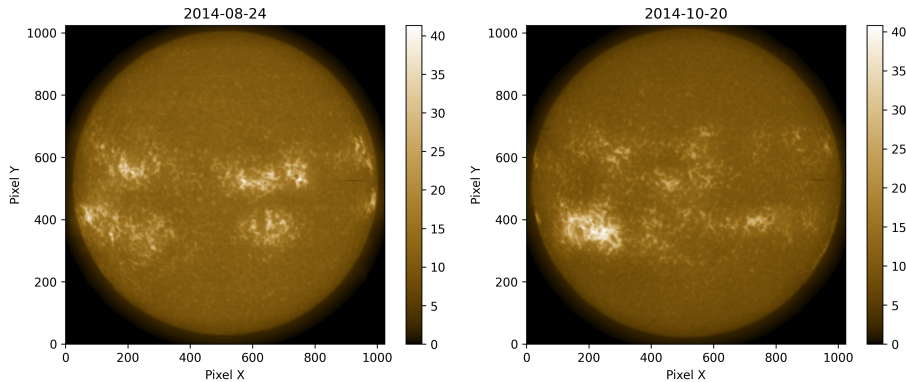


Figure 6. The final mock SUII images after binning the working samples in Fig. ?? to 1024×1024 .

of the bounding box, and our model outputs the coordinates of the bounding box for each feature.

The original mock-SUII images are ≈ 200 images, which contains both psf-convolved and non psf-convolved images. While the usual norm is to consider the original data arrays, 200 images do not constitute a sufficient dataset for training a deep learning model. Hence, to perform effective data augmentation, we save the data as lossless JPG images, and perform several data augmentations as listed below. This results in ≈ 3056 images, which we use for training the model. The augmentation performed on the training images are:

- **Gray Scale Conversion:** The color image is converted to a grayscale image.
- **HSV conversion:** HSV (Hue, Saturation, Value) conversion is a color representation model that separates image color information into three components: hue (the color type), saturation (the intensity or purity of the color), and value (the brightness of the color). We converted the images from RGB to HSV space, where hue is mapped between 0 and 179, each channel having a unique value, while saturation varies between 0 and 255.
- **Gamma Variations:** The brightness of the images are varied by changing the γ value as per Eq. 1. We varied γ as 0.2, 0.4, 0.6, 0.8 and chose the best looking ones. The augmentations were performed as:

$$image = [image]^\gamma \quad (1)$$

These gamma variations serve to make the model robust to intensity variations occurring due to in-flight performance of SUII. However, we do not select the full range of γ for augmentation, and select only the images which do not look starkly different from the source images, through visual inspection.

- **Vertical and Horizontal Flips.**

The resultant set of augmentations are shown in Fig. 7.

We evaluate the model on a validation set with ≈ 123 data, in FITS format. Note that to obtain a 3-channel image of our model, we replicate the mock

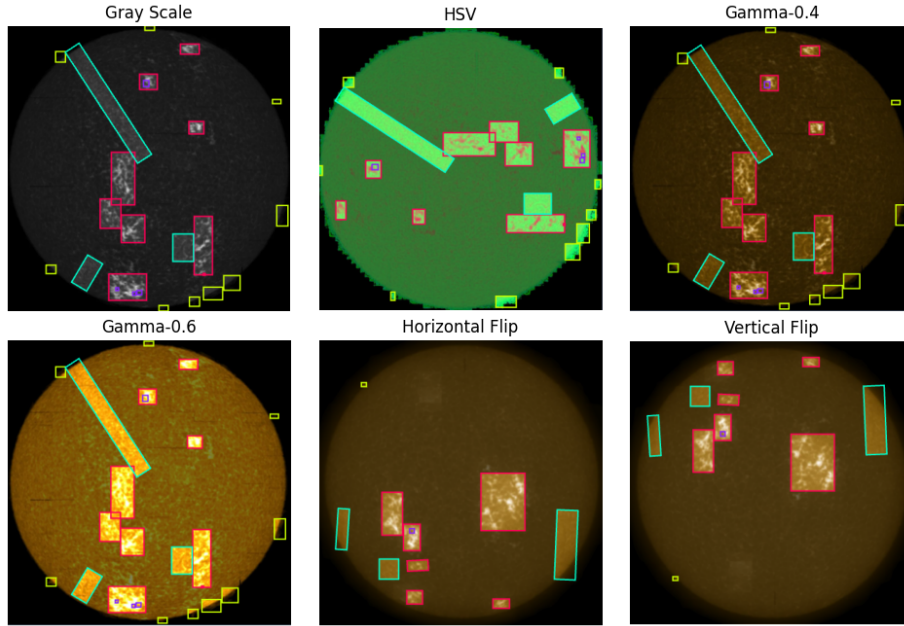


Figure 7. Example representative augmentation for an example mock SUI image. Starting from the top-left and moving clockwise, the transformations include: Gray Scale conversion, HSV conversion, $\gamma = 0.4$, vertical and horizontal flip, and $\gamma = 0.6$.

Table 1. Number of samples in the dataset.

Dataset	No. of samples
Pre-augmentation samples	217
Post augmentation train samples	3056
Post augmentation validation (JPG) samples	297
Validation samples(FITS)	123
Test samples-SUIT Data (FITS)	92

SUIT image into all the three RGB channels. These data are used to evaluate the model weights. Finally, the testing set in our case are the actual SUI Level 1 2k data. The details for the complete dataset are mentioned in Table 1.

SUIT Level 1 data are science-ready FITS images, generated from Level 0 (uncorrected) data. Bias correction, flat field correction, scattered light removal, and dark removal are performed, followed by orientation correction and WCS implementation of the Sun images. [34].

Once the data are ready, we normalize the data across the mock-SUIT and SUI data. We subtract each image by its minimum value, divide by the range, and then multiply it by 255 to ensure compliance with 8-bit image representation.

3. Model architecture and evaluation

SPACE is based on the architecture of You Only Look Once (YOLO)[37][45], containing a backbone of a Convolutional Neural Network (CNN). The YOLO series of models contains a backbone, neck, and head. It ingests RGB images and outputs the bounding boxes for each feature, along with the probability of the feature in consideration. Here, we have utilized two versions of YOLO, v8 [37, 20] and v9 [45]. In the YOLO-v8, we also consider the v8-mobb and v8-m models. The v8-mobb model considers the input coordinates in the OBB format. In contrast, the v8-m model considers the bounding boxes in traditional axis-aligned scheme. We refer to the v8 papers for details on the model architectures [37, 20].

We consider the following target classes: “Plages”, “Sunspots”, “Filaments” and “Off-limb features”. We trained the models for 500 epochs, with a batch size of 8, and a combination of multiple loss functions. YOLOv8 has a loss function consisting of three terms: bounding box regression loss (L_{box}), confidence loss (L_{conf}), and classification loss (L_{class}) as shown in Eq. 2.

$$\mathcal{L}_{\text{YOLOv8}} = \mathcal{L}_{\text{box}} + \mathcal{L}_{\text{conf}} + \mathcal{L}_{\text{class}} \quad (2)$$

Yolov8 utilizes CIoU (Complete Intersection over Union) to calculate the box regression loss (\mathcal{L}_{box}). It improves upon traditional IoU by considering additional factors such as the Euclidean distance between the centers of the predicted and ground truth bounding boxes, the aspect ratio, and the scale of the boxes. This can be expressed mathematically as:

$$L_{\text{CIoU}} = 1 - \text{IoU} + \frac{\rho^2(b, b_{\text{gt}})}{c^2} + \alpha v$$

$$\mathcal{L}_{\text{box}} = 1 - \text{CIoU}$$

IoU refers to the standard intersection over union measure, $\rho(b, b_{\text{gt}})$ represents the Euclidean distance between the center points of the predicted bounding box b and the ground truth bounding box b_{gt} . The term c is the diagonal length of the smallest enclosing box that can contain both the predicted and ground truth boxes, and α is a constant that controls the penalty for aspect ratio differences, where v represents the aspect ratio similarity.

The confidence loss ($\mathcal{L}_{\text{conf}}$) is defined as

$$\mathcal{L}_{\text{conf}} = \sum \mathbf{1}_{ij}^{\text{obj}} (C_{ij} - \hat{C}_{ij})^2 + \lambda_{\text{noobj}} \sum \mathbf{1}_{ij}^{\text{noobj}} (C_{ij} - \hat{C}_{ij})^2$$

where C_{ij} are the confidence scores of each pixel in GT, \hat{C}_{ij} are the confidence scores in the predicted bounding box. *obj* and *noobj* correspond to locations consisting and not-consisting of a bounding box respectively. This loss term evaluates how well the model predicts whether a bounding box contains an object, ensuring reliable objectness predictions.

Lastly, the classification loss (\mathcal{L}_{class}) is defined as:

$$\mathcal{L}_{class} = \sum \mathbf{1}_{ij}^{obj} \sum_{c=1}^C (p_{ij}(c) - \hat{p}_{ij}(c))^2,$$

where $p_{ij}(c)$ corresponds to the probability of each predicted class, and \hat{p} is the predicted probability by the model. This term determines the accuracy of the model in assigning the correct class label to detected objects.

In the v8-obb model, the loss function is defined as:

$$\mathcal{L}_{OBB} = \mathcal{L}_{box} + \mathcal{L}_{angle}(\theta_i, \hat{\theta}_i) + \mathcal{L}_{conf} + \mathcal{L}_{class},$$

where the loss term includes an additional term to account for the orientation of the bounding boxes. The additional loss term $\mathcal{L}_{angle}(\theta_i, \hat{\theta}_i)$ is defined as

$$\mathcal{L}_{angle}(\theta_i, \hat{\theta}_i) = \min(|\theta_i - \hat{\theta}_i|, 2\pi - |\theta_i - \hat{\theta}_i|),$$

where the loss term compares the angular error between the predicted and ground truth angles ($\hat{\theta}_i$ and θ_i). This angular loss is designed to handle the periodic nature of angles, ensuring smooth error calculations even at boundary conditions (e.g., 0° vs 360°).

YOLOv9's loss function is a combination of CIoU loss by default as mentioned above, objectness loss and classification loss.

Objectness loss evaluates how well the model predicts the presence of an object in a bounding box. It is computed using binary cross-entropy, which quantifies the difference between the predicted and actual objectness labels. The objectness loss is defined as:

$$L_{obj} = - \sum_{i \in \text{boxes}} [p_{obj} \log(\hat{p}_{obj}) + (1 - p_{obj}) \log(1 - \hat{p}_{obj})]$$

p_{obj} is the ground truth label indicating the presence of an object. \hat{p}_{obj} is the predicted probability that the bounding box contains an object.

Classification loss evaluates the accuracy of the model's class predictions. It is typically calculated using categorical cross-entropy, which penalizes the difference between the predicted class probabilities and the actual class labels. The classification loss is given by:

$$L_{class} = - \sum_{i \in \text{objects}} y_i \log(\hat{y}_i)$$

where, y_i is the one-hot encoded ground truth label for class i and \hat{y}_i is the predicted probability for class i .

The final total loss function for YOLOv9 is a weighted combination of these components:

$$L_{total} = L_{CIoU} + \lambda_{obj} L_{obj} + \lambda_{class} L_{class}$$

where λ_{obj} and λ_{class} are hyperparameters that control the importance of the objectness and classification losses in the total loss.

Both models used Stochastic Gradient Descent (SGD) as an optimizer, with a learning rate of 0.01 [37, 45].

3.1. Model evaluation

We use a couple of metrics to evaluate our model performance for various IoU:

- Precision: A measure of the fraction of classified positive samples which are classified correctly, defined as:

$$\text{Precision} = \frac{\text{TruePositive}}{\text{TruePositive} + \text{FalsePositive}} \quad (3)$$

- Recall: A measure of the number of positive samples correctly classified, defined as:

$$\text{Recall} = \frac{\text{TruePositive}}{\text{TruePositive} + \text{FalseNegative}} \quad (4)$$

- Mean Average Precision (MAP): AP is the average precision of each class, while MAP is the mean of AP, defined as:

$$mAP = 1/N \sum AP_i \quad (5)$$

4. Evaluation strategy: statistical and Tamura measures

In this work, we have manually identified the bounding boxes for each feature in the mock SUIT images. For the given bounding boxes, we would like to have a more objective set of measures for determining the different regions of interest. Specifically, this is also needed in the absence of a GT in the SUIT images, to verify if the features we recover statistically are consistent with the class labels. Visually, these different morphological regions appear different because of differences in the intensity distribution. Hence, we compute statistics of intensity distribution within the bounding boxes. We define 10 such parameters, collectively calling them *Feature properties*:

1. Entropy: For a probability distribution $P(x)$, the Shannon entropy[10] is defined as: $-\sum P(x_i) \log P(x_i)$. This provides a measure of ‘non-peaked-ness’ of the intensity distribution.
2. Standard Deviation (σ): $\sqrt{\frac{\sum(x_i - \bar{x})^2}{N}}$, where \bar{x} is the mean intensity in the bounding box and N denotes the sample size.
3. Skewness: It is a measure of the asymmetry of the pixel intensity distribution, and is the third central moment of an image. The skewness is calculated as:

$$N \cdot \sum_{i=1}^N (x_i - \bar{x})^3 / ((N - 1)(N - 2) \cdot \sigma^3),$$

where N , x_i , \bar{x} , σ denotes the sample size, individual data points, mean, and standard deviation, respectively.

4. Kurtosis: It is a measure of the occurrence rate and magnitude of the anomalies and is the fourth central moment. The kurtosis is measured as:

$$N \cdot (N + 1) \cdot \sum_{i=1}^N (x_i - \bar{x})^4 (N - 1) \cdot (N - 2) \cdot (N - 3) \cdot \sigma^4 - \frac{3 \cdot (N - 1)^2}{(N - 2) \cdot (N - 3)},$$

where N , x_i , \bar{x} , σ denotes measure sample size, individual data points, mean, and standard deviation, respectively.

Our other measures include the Tamura properties computed for each feature. The Tamura properties refer to measurements of differences in texture characteristics such as coarseness, contrast, roughness, etc. In this work, we use the Tamura properties to identify textural patterns along 0, 45, and 90-degree orientations. We calculate the Grey Level Correlation Matrix (GLCM)[17] for each bounding box, and define our metrics. For each element P_{ij} in GLCM we define:

5. Contrast: $\sum P_{ij}(i - j)^2$
6. Homogeneity: $\sum P_{ij}/1 + P_{ij}(i - j)^2$
7. Dissimilarity: $\sum P_{ij}(i - j)$
8. Energy: $\sqrt{\sum P_{ij}^2}$
9. Correlation: $\sum P_{ij}[(i - \mu_i)(j - \mu_j)]/\sqrt{\sigma_i^2 \sigma_j^2}$

These set of metrics are computed for each bounding box in the training, validation and testing sets, for interrogation of both the labels and model detections.

5. Results

In this section, we present the results of our developed models, and also present the comparative study of *Feature properties* for the Ground truth, Predictions, and SUI data.

5.1. Visual Detection

5.1.1. Model performance on mock SUI data

We validate the final models YOLO-v8, YOLO v8-obb, and YOLO-v9 using the mock SUI data, as mentioned in Section 2. We present the validation on the JPG images. These numbers are presented in Table. 2. From these metrics, we find the model v8-obb to be the best model for the task at hand. Hence, we consider the obb model as our main model for **SPACE**.

We now consider the FITS data, and present performance of the v8-obb model on these FITS data in Table. 3, for each class label. The first row of Table. 3 contains the summary statistic of all features, and can be compared with the

first row of Table. 2. We find that the model performance to be better with JPG over FITS data. This arises because the JPG data are (i). Lossy, and (ii). Quantized as integers. Hence, very subtle variations in intensity are washed out due to the JPG compression, which results in a better performance in JPG over FITS data.

Comparing the model performance for different features in Table. 3, we find that the model shows excellent recall in most cases, except for off-limb regions. The precision is best for filaments and plages, and lesser for sunspots and off-limb regions. We present inference on two SUIE mock examples with the inputs taken in the native FITS format, and show them in Fig. 8.

Table 2. Comparison of the validation results on the JPG data for all models.

JPG					
Models	Precision	Recall	Mean Average Precision [0-50] (MAP)	Mean Average Precision [50-95] (MAP)	
v8obb	0.85077	0.99546	0.97217		0.90361
v8	0.78675	0.98475	0.94937		0.84687
v9	0.79491	0.97812	0.94705		0.82481

Table 3. Validation results for the selected v8-obb model on the FITS data.

Class labels	Precision	Recall	Mean Average Precision [0-50] (MAP)	Mean Average Precision [50-95] (MAP)
all	0.788	0.863	0.874	0.819
filament	0.78	0.96	0.934	0.906
off-limb	0.875	0.542	0.751	0.63
plages	0.716	0.985	0.922	0.905
sunspot	0.783	0.965	0.889	0.834

5.1.2. Model Deployed on the real SUIE Data

In Fig. 9, we present the performance of our best model which is v8m-obb mentioned above on the observed SUIE data. The panel contains two sets of images compared with sunspot identification from the 1700 Å passband of the Atmospheric Imaging Assembly (AIA) [24, 7] onboard Solar Dynamics Observatory (SDO) [31]. The first row shows the SUIE images with the bounding boxes inferred by rescaling each image by subtracting the minimum and dividing by the range of intensities, as is the standard scheme of rescaling for image data. For such an image, we find that the model fails to capture many of the small-scale structure, especially the sunspots, while comparing the estimated sunspots with the AIA data. We perform a trial and error of rescaling, and find that a rescaling of each image by a factor of 8 helps in better identification of

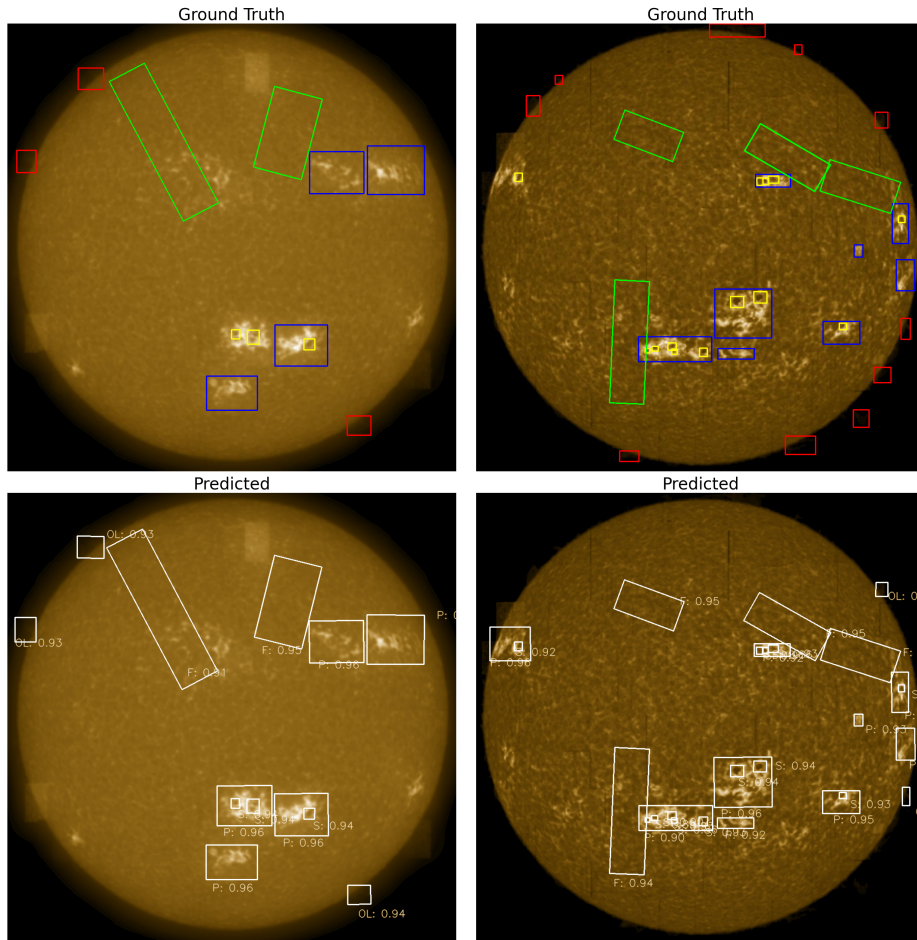


Figure 8. Predictions on SUIE MOCK FITS. F: Filaments, OL: Off Limb features, S: Sunspots P: Plages. The numbers in each box present the confidence score calculated for each feature between 0 and 1. The images shown were observed on October 13th, 2013 (right column) and September 9th, 2021 (left column). Top panels are the ground truth data, depicting the manually labeled bounding boxes. Bottom panel depict the inference from the model for the same images.

the features in the SUIE images. These estimated boxes are shown in the second row of Fig. 9.

First off, we find that the SUIE observations show several features of interest. The model is able to capture several plage regions very well with high confidence – for instance, the big plage in the southern hemisphere in the left column of Fig. 9 is captured with a confidence of > 0.8 . Second, we see several sunspots being captured by the model. Interestingly the model seems to have a wide range of confidence levels in capturing these sunspots. This may occur due to a significant perceptual contrast difference between the mock and real SUIE images. In fact, we find the large plage region in the northern hemisphere of the left panel is not captured by the model – this effect could arise from the contrast,

and a lack of such a strongly oriented feature in the training set. We note that the level 1.1 SUI data are scattered light and flat field corrected, and have been recorded with an exposure time of 1.4 seconds. However, there are variations in intensity over time as the net throughput changes due to contaminant deposition on the CCD. This gets cleaned after every baking cycle, until it gets dim again. This inconsistency of throughput is not captured by the training set and the model, and hence a manual normalization is necessary at the moment.

5.2. Evaluation using statistical and Tamura measures

We now perform a comparative analysis of the *Feature parameters*. The counts of these individual features, both ground truth and predicted, are given in Table 4. These regions are chopped out, using the detected coordinates from the original FITS data and not the rescaled data, to ensure that we capture the non-altered values. Hence, some of the numbers may not be precisely comparable between the mock-SUIT and SUI data.

Table 4. Detected Events

	Plages	Sunspots	Filaments	Off-limb
Training Set (Ground Truth)	65	42	46	52
Training Set (Predicted)	1044	484	315	915
Validation Set (Ground Truth)	46	26	31	33
Validation Set (Predicted)	564	310	161	237
Test(SUIT Data)	420	251	NA	42

In Fig. 10, we present the distribution of Entropy, σ , skewness, and kurtosis computed within each bounding box for the training set (GT and prediction), validation set (GT and prediction), and SUI data. The different colors correspond to different features of interest.

From the first row of Fig. 10, we find that entropy clearly differentiates between the four features. We find that distributions for predictions align fairly well with the ground truth for both training and validation sets. We find that the sunspots have a lower entropy than plages, which have lower entropy than filaments. The sunspots in our bounding boxes are seen with almost similar intensities in the box, while in plages, we see far more structure and intensity variation. The filament bounding boxes encompass a large area, with most of the bounding box consisting of non-filamentary structures with varied intensities. Since entropy is a measure of the number of non-unique intensities in each feature, we find the entropy distributions in the increasing order of sunspots, plages and filaments in Fig. 10 first row. We note that the off-limb structures lie somewhere between sunspots and plages in the dataset. However, the SUI-pred panel shows a notable increase in the location of the peak of the distribution for plages and off-limb regions, suggesting some inconsistency in model predictions on real SUI data.

From the second row of Fig. 10, we find that the standard deviation σ spans a wide range across all data. Predictions for standard deviation appear relatively

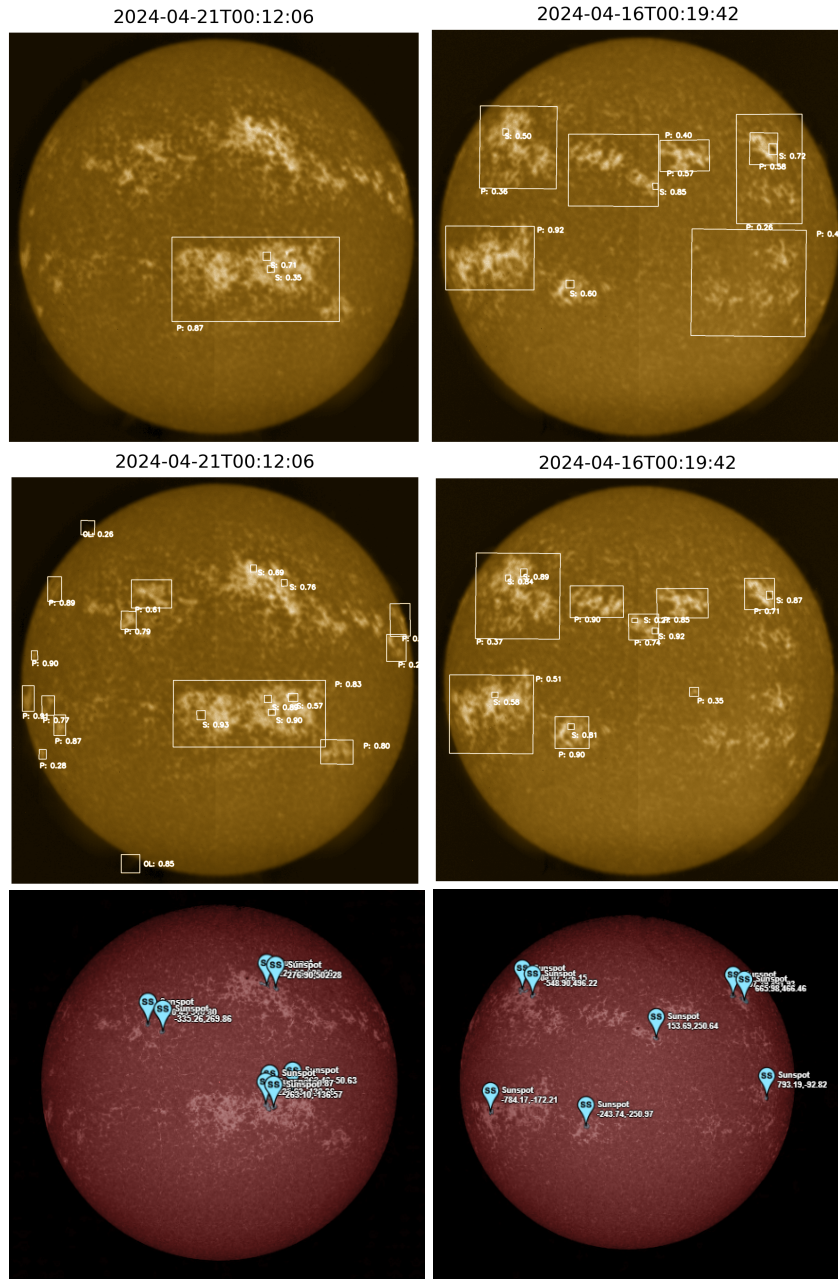


Figure 9. Inference on SUII Images (top two panels) and reference AIA 1700 images (bottom panel). The features are given as: F: Filaments, OL: Off Limb features, S: Sunspots P: Plages; Confidence Score calculated for each event, whose value lies between 0 and 1. The top row corresponds to inference using the min-max image rescaling, while the middle row corresponds to inference using im/8 rescaling.

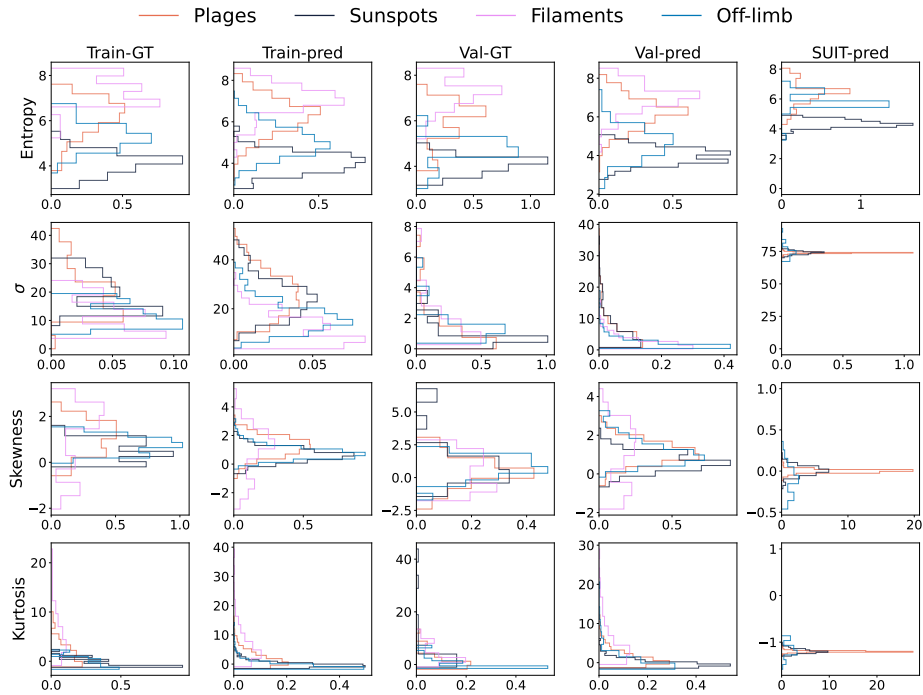


Figure 10. Variation of the statistical measures for the features of interest, in terms of entropy, σ , skew and kurtosis along each row. The columns correspond to the train ground truth, train prediction, validation ground truth, validation prediction, and SUI prediction respectively. Sunspots are marked with dark-gray color, plages with yellow-orange color, filaments with pink and off-limb regions with blue color.

consistent with the ground truth across training and validation sets. The distribution of σ however changes in the SUI data, with all the distributions being more consistent with each other. If we were to consider only the median values of the distribution, they are mostly consistent across all of the datasets. Thus, standard deviation does not seem to be a very good discriminator of the selected features, and does not aid us in an auto-validation procedure.

In the third row of Fig. 10, we present the skewness of the intensities in different bounding boxes. In the training set, we find the filament intensity skewness to span a wide range, while the other features show a distribution peaked near 0, but on the positive side. This is also noticed in the prediction from the training set. In the validation set, we find the skew to be mostly positive, with the predictions consistent with the ground truth. The SUI skew are similarly peaked near 0, but we find that the off-limb structures have a large spread of skew values unlike the mock dataset. The intensity distribution in any of the features of interest generally has a long tail towards the higher end than the lower end, and this is captured by the skewness. However, we note that the skewness of intensity distribution is again not a good discriminator of the selected features, and does not aid us in an auto-validation procedure.

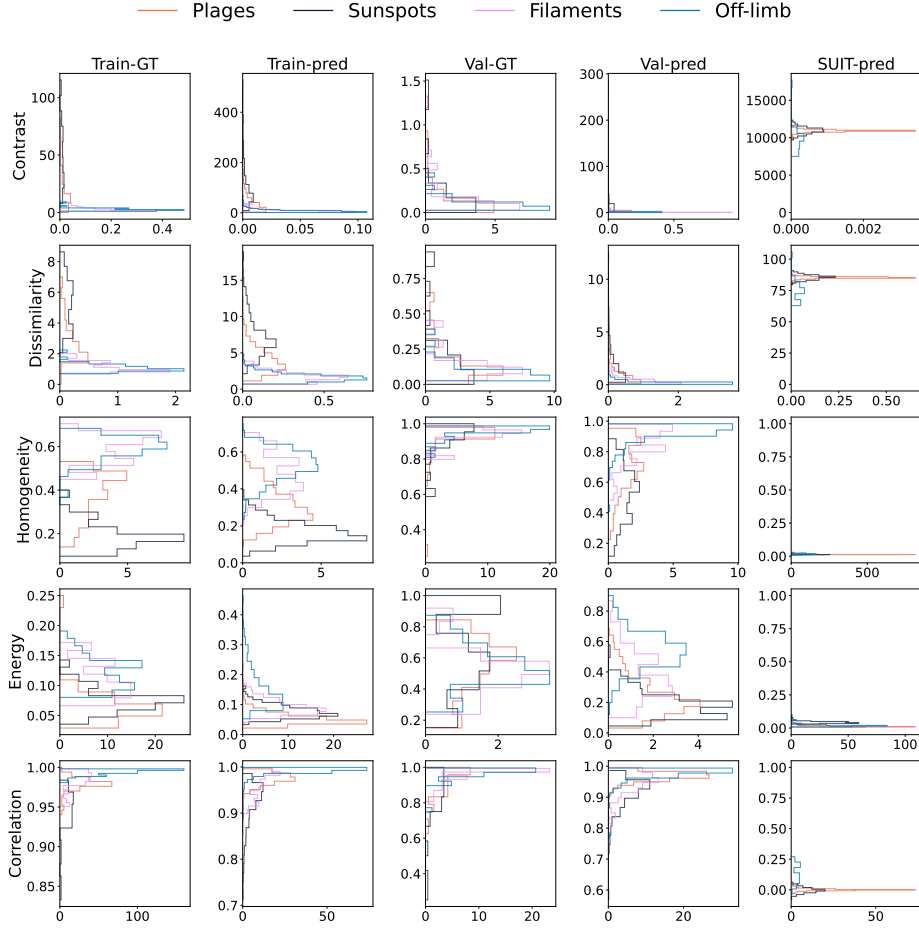


Figure 11. Variation of the Tamura measures for the features of interest, including contrast, dissimilarity, homogeneity, energy, and correlation. The columns correspond to the train ground truth, train prediction, validation ground truth, validation prediction, and SUII prediction respectively. Sunspots are marked with dark-gray color, plages with yellow-orange color, filaments with pink and off-limb regions with blue color.

In the final row of Fig. 10, we present the kurtosis of the intensity distribution in the different bounding boxes. In general, we find a good agreement in kurtosis distributions between predictions and ground truth for training and validation data. We find that the filaments and plages tend to have more samples with larger kurtosis, indicating a distribution falling off faster than a Gaussian. This seems to reflect a very long tail of intensities, which is also consistent with the higher entropy of these regions from the first row of this figure. However, the kurtosis for SUII-pred data exhibits tighter and sharper peaks, while having the opposite sign. This indicates a potential underestimation of tails in intensity distributions, particularly in off-limb areas. Furthermore, this is also reflective of the difference in the mock-SUII and real-SUII observations, which are seen as inconsistencies here.

Overall, we find that the model shows reasonable performance in replicating training and validation data distributions. While the actual values of these statistical measures are different with SUI data, the distributions are mostly consistent across mock SUI and SUI predictions. We note that the divergence of results occurs especially in the off-limb regions.

In Fig. 11, we present the distributions of contrast, dissimilarity, homogeneity, energy, and correlation measures for each bounding box, as described in §. 11. These are computed within each bounding box for the training set (GT and prediction), validation set (GT and prediction), and SUI data. The different colors correspond to different features of interest, given here as sunspots (dark gray), plages (yellow-orange), filaments (pink), and off-limb regions (blue).

In the first row of Fig. 11, we display the contrast across the different features. The ground truth contrast distributions for training and validation data show relatively low contrast values across structures, especially for plages, sunspots, and off-limb regions. The model captures this in training and validation predictions, though there is some spread in SUI-pred. However, we note that the contrast values are larger in sunspots, when compared to plage and filament regions. Interestingly, the absolute contrast values are 2 orders of magnitude larger in the SUI images, which point to differences in the actual values of the mock and real SUI data. We also note that the distribution in SUI boxes itself is quite symmetric, unlike the mock data.

In the second row of Fig. 11, we display the dissimilarity for the different features of the datasets. We again find a distinction in the distributions for mock-SUI and SUI data. We find the dissimilarity in training and validation data are generally well-aligned between ground truth and predictions. In the mock-SUI data, we find sunspots to have higher dissimilarity over plage and filament regions. However, sunspots also have low entropy from the first row of Fig. 10. This tells us that the dissimilarity is large in sunspots due to an emphasis of the metric on boundaries. The core structures themselves, are, however of similar intensities, which results in a lower entropy of the first row of Fig. 10.

In the third row of Fig. 11, we display the homogeneity of the for different features. We find each feature to present a distinct distribution across all data. We see that sunspots are the least homogeneous, followed by plage, offlimb structures, and filaments. The absolute homogeneity numbers are however less for SUI observations. The model distribution from predictions well-match the ground truth. Homogeneity, while not complete, can be used as a measure to differentiate between these features.

In the fourth row of Fig. 11, we display the energy of the images. Essentially, the energy reflects the concentration of certain intensity values. We find off-limb and filaments to have higher energy. However, this is flipped in the SUI images, with sunspots showing as an outlier distribution. Furthermore, SUI-pred shows substantially lower energy values across all structures, particularly off-limb areas.

Finally, we present the correlation measure in the last row of Fig. 11. We find the features to have similar autocorrelation datasets in mock-SUI, and this changes in SUI data. The correlation values are quite high for all structures in training and validation data, indicating a consistent spatial relationship between neighboring pixels. Predictions align well with the ground truth for these

datasets. SUIT-pred, however, exhibits lower correlation values, particularly for off-limb regions, suggesting that the model may be struggling with accurately predicting spatial relationships in Mg II k passband images.

Overall, we find a good consistency between the *feature properties* of the GT and the predicted bounding boxes for the mock SUIT data. Furthermore, we also find a good consistency between the mock SUIT and SUIT data in several of the *feature properties*.

6. Discussion and conclusions

In this work, we have developed **SPACE**, an event detection system for SUIT. Specifically, we develop a system to identify sunspots, filaments, plage and off-limb regions. This framework is based on a YOLO v8obb model, and is trained on mock-SUIT data generated from IRIS mosaics. We perform a comparison across different YOLO versions, and select the best performing model for our feature identification purposes. The best model achieves a precision of 0.85, recall of 0.99, and an MAP of 0.97 and 0.90 on JPG files and a precision of 0.79, recall of 0.86, and an MAP of 0.87 and 0.82 for FITS data respectively.

We deploy this system on SUIT data, and find that the model picks up most of the regions of interest, if we perform a visual inspection. However, since the GT is generated by hand-labeling individual features of interest, the system lacks a more objective measure of determining model performance on actual SUIT images in the absence of a ground truth dataset.

To this end, we develop a self-validation scheme based on statistical and Tamura measures, which provide a comparison of these measures across different features of interest. These features are based on the statistical moments and grey-level correlation matrix for the intensity values for each feature, described in §. 4. The proposed metrics capture various properties of the intensity distributions for our features of interest. A statistical distribution of these metrics for the GT and predicted bounding boxes for different features, along with the metrics for SUIT data would enable an automatic self-validation of the performance of the model. We perform this analysis and note the results in §. 5.

We find entropy to be the best metric statistically differentiating the features of interest. The distribution of entropy for all samples follows similar trends across both the ground truth and predictions of mock-SUIT and SUIT data. This gives us confidence in the performance of our model on unseen data, and lets us perform a zero-shot learning of SUIT data.

Among the other metrics considered, we find contrast, dissimilarity, homogeneity and energy to also provide an understanding of the differences between the features. While the distribution of these metrics have a great overlap across the different features, some of the features have strong signals that help us understand the consistency across all dataset.

We find that sunspots exhibit low entropy, high dissimilarity and contrast, and low homogeneity and correlation across all datasets. Since sunspots are structures with uniform intensity, there are not many ‘unique’ pixel intensities, and this results in a relatively lower entropy when compared to other features.

However, this is in tension with high dissimilarity and contrast, which are also measures of the number of non-unique pixel intensities in the region of interest. The sunspots, due to sharp intensity changes at the boundary, result in a high dissimilarity and contrast, but lower entropy. We note that while the energy is generally consistent with other features, the SUI data and the validation GT shows sunspots with high energy, corresponding to several similar intensity values, reflecting the entropy of the intensities. Finally, the low homogeneity and correlation are possibly the effect of the boundaries, which may wrongly lead us to interpret sunspots as regions with a lack of spatial uniformity.

We find that the filaments display high entropy and mild dissimilarity, low contrast, medium homogeneity and correlation, high positive and negative skewness, and high kurtosis. The filaments are long structures, with their bounding boxes encompassing both the filament and surrounding regions. This highlights their complex, varied textures and uneven intensity transitions across the structure, and hence are seen as features with high entropy. Since the filaments in mock-SUIT data are seen very weakly, we see these structures with lower contrast than plage or sunspot regions, reflecting more gradual intensity changes without sharp boundaries. Since the filament regions contain a lot of background + the filament, these regions have low homogeneity and correlation, indicating inconsistent intensity patterns and less predictable pixel relationships across the structure. We note the rather high skewness and kurtosis for filaments arise from the different kinds of background they can have, resulting in intensity distributions with a long tail or sharp peaks.

Plages are regions with relatively uniform, and bright intensities. These are captured by our metrics as low entropy, low dissimilarity, high homogeneity, and high correlation. They also have high contrast which reflects subtle variations in brightness within plages rather than abrupt transitions. They also show moderate skewness and kurtosis, indicating a somewhat peaked but symmetrical intensity distribution.

The off-limb regions are defined as structures seen outside the disc of the Sun. These regions could be any intensity structures, but are most probably prominences. These off-limb regions have low entropy, low contrast, and high homogeneity, capturing their relatively empty and uniform background intensity. Low dissimilarity and correlation indicate consistent intensity patterns without structured variations. They also have very low skewness, that reflect the uniform, low-intensity nature of these regions, with minimal brightness variation.

The proposed auto-validation scheme evaluates the extracted correctness of the bounding boxes. It does not, however, provide a measure of the fraction of all regions captured correctly by the model. For this purposes, we will again need to resort to manual labeling of data.

In summary, we find that we can explain the behavior of these measures with our features of interest, and this behavior is consistent with known observations. With such measures of comparison, we find that the model performs well in capturing statistical and Tamura measures for the training and validation datasets. However, many of the numbers are very different from the actual SUI data, which is likely due to the discrepancy between the scheme for mock-SUIT image generation, and the SUI images themselves. We note that a deployment

of this model would need fine-tuning on real SUIE data for a more effective identification of features. We plan to perform a semi-supervised training of the SPACE model using the labelled SUIE data with a human-in-loop system, while having a continuous learning framework to account for changes in SUIE data over time. Adjusting the model to better account for these differences will improve generalization to SUIE data, especially for complex structures like filaments and off-limb regions.

Acknowledgements P.S. would like to thank the Inter-University Centre for Astronomy and Astrophysics, Pune for providing support during his research visit. U.V and D.T would like to acknowledge funding from ISRO/RESPOND for the project “Solar Flares: Physics and Forecasting for Better Understanding of Space Weather”, ISRO/RES/2/438/22-23. U.V. and D.T. would like to acknowledge the NVIDIA Academic Hardware grant provided to U.V. and IUCAA. U.V. would like to thank Carlos Diaz Baso for comments and suggestions on the work and manuscript.

Aditya-L1 is an observatory class mission which is funded and operated by the Indian Space Research Organization. The mission was conceived and realised with the help from all ISRO Centres and payloads were realised by the payload PI Institutes in close collaboration with ISRO and many other national institutes - Indian Institute of Astrophysics (IIA); Inter-University Centre of Astronomy and Astrophysics (IUCAA); Laboratory for Electro-optics System (LEOS) of ISRO; Physical Research Laboratory (PRL); U R Rao Satellite Centre of ISRO; Vikram Sarabhai Space Centre (VSSC) of ISRO. SUIE is built by a consortium led by the Inter-University Centre for Astronomy and Astrophysics (IUCAA), Pune, and supported by ISRO as part of the Aditya-L1 mission. The consortium consists of SAG/URSC, MAHE, CESSI-IISER Kolkata (MoE), IIA, MPS, USO/PRL, and Tezpur University. IRIS is a NASA small explorer mission developed and operated by LMSAL with mission operations executed at NASA Ames Research Center and major contributions to downlink communications funded by ESA and the Norwegian Space Centre.

This research used Numpy [44], Scikit-image [40], Open-CV [9], pillow [11], pytorch [30], torchvision [26], seaborn [46], ultralytics [20, 45], astropy [32], scipy [42], sunpy [27], matplotlib [19] python libraries.

Appendix

Code Availability The Github repository, containing the complete code structure is attached here. ⁴ The repository would be made public once the journal’s review process is complete.

Declarations

Conflict of interest The authors declare they have no conflicts of interest.

References

- [1] Azim Ahmadzadeh, Dustin J. Kempton, Michael A. Schuh, and Rafal A. Angryk. Improving the functionality of tamura directionality on solar images. In *2017 IEEE International Conference on Big Data (Big Data)*, pages 2518–2526, 2017.
- [2] Azim Ahmadzadeh, Sushant S. Mahajan, Dustin J. Kempton, Rafal A. Angryk, and Shihao Ji. Toward Filament Segmentation Using Deep Neural Networks. *arXiv e-prints*, page arXiv:1912.02743, November 2019.

⁴<https://github.com/pranava1709/Event-Detection-System-for-SUIE-Data.-/tree/master/>

-
- [3] Juan M Banda, Chang Liu, and Rafal A Angryk. Region-based querying of solar data using descriptor signatures. In *2013 IEEE 13th International Conference on Data Mining Workshops*, pages 1–7. IEEE, 2013.
- [4] T. Barata, S. Carvalho, I. Dorotovič, F. J. G. Pinheiro, A. Garcia, J. Fernandes, and A. M. Lourenço. Software tool for automatic detection of solar plages in the Coimbra Observatory spectroheliograms. *Astronomy and Computing*, 24:70, July 2018.
- [5] A. Benkhalil, V. V. Zharkova, S. Zharkov, and S. Ipson. Active Region Detection and Verification With the Solar Feature Catalogue. *Solar Physics*, 235(1-2):87–106, May 2006.
- [6] M. Bertalmio, A.L. Bertozzi, and G. Sapiro. Navier-stokes, fluid dynamics, and image and video inpainting. In *Proceedings of the 2001 IEEE Computer Society Conference on Computer Vision and Pattern Recognition. CVPR 2001*, volume 1, pages I–I, 2001.
- [7] Paul Boerner, Christopher Edwards, James Lemen, Adam Rausch, Carolus Schrijver, Richard Shine, Lawrence Shing, Robert Stern, Theodore Tarbell, Alan Title, C. Jacob Wolfson, Regina Soufli, Eberhard Spiller, Eric Gullikson, David McKenzie, David Windt, Leon Golub, William Podgorski, Paola Testa, and Mark Weber. Initial Calibration of the Atmospheric Imaging Assembly (AIA) on the Solar Dynamics Observatory (SDO). *Solar Physics*, 275(1-2):41–66, January 2012.
- [8] Slava Bourgeois, Teresa Barata, Robertus Erdélyi, Ricardo Gafeira, and Orlando Oliveira. Sunspots Identification Through Mathematical Morphology. *Solar Physics*, 299(2):10, January 2024.
- [9] G. Bradski. The OpenCV Library. *Dr. Dobb's Journal of Software Tools*, 2000.
- [10] Ricky Chen. A brief introduction on shannon's information theory, 01 2016.
- [11] Alex Clark. Pillow (pil fork) documentation, 2015.
- [12] T. Colak and R. Qahwaji. Automated McIntosh-Based Classification of Sunspot Groups Using MDI Images. *Solar Physics*, 248(2):277–296, April 2008.
- [13] Bart De Pontieu, JR Lemen, GD Kushner, DJ Akin, B Allard, T Berger, P Boerner, M Cheung, C Chou, JF Drake, et al. The interface region imaging spectrograph (iris). *Solar Physics*, 289(7):2733–2779, 2014.
- [14] Andrea Diercke, Robert Jarolim, Christoph Kuckein, Sergio J. González Manrique, Marco Ziener, Astrid M. Veronig, Carsten Denker, Werner Pötzi, Tatiana Podladchikova, and Alexei A. Pevtsov. A universal method for solar filament detection from H α observations using semi-supervised deep learning. *Astronomy & Astrophysics*, 686:A213, June 2024.
- [15] Suruchi Goel and Shibu K. Mathew. Automated Detection, Characterization, and Tracking of Sunspots from SoHO/MDI Continuum Images. *Solar Physics*, 289(4):1413–1431, April 2014.
- [16] Xulong Guo, Yunfei Yang, Song Feng, Xianyong Bai, Bo Liang, and Wei Dai. Solar-Filament Detection and Classification Based on Deep Learning. *Solar Physics*, 297(8):104, August 2022.
- [17] Mryka Hall-Beyer. Gcm texture: A tutorial v. 3.0 march 2017, 03 2017.
- [18] T. Huang, G. Yang, and G. Tang. A fast two-dimensional median filtering algorithm. *IEEE Transactions on Acoustics, Speech, and Signal Processing*, 27(1):13–18, 1979.
- [19] John D Hunter. Matplotlib: A 2d graphics environment. *Computing in science & engineering*, 9(3):90–95, 2007.
- [20] Glenn Jocher, Ayush Chaurasia, and Jing Qiu. Ultralytics yolov8, 2023.

-
- [21] Dustin Kempton, Karthik Ganesan Pillai, and Rafal Angryk. Iterative refinement of multiple targets tracking of solar events. In *2014 IEEE International Conference on Big Data (Big Data)*, pages 36–44, 2014.
- [22] Dustin J. Kempton, Michael A. Schuh, and Rafal A. Angryk. Tracking Solar Phenomena from the SDO. *The Astrophysical Journal*, 869(1):54, December 2018.
- [23] Haruka Kido. Image inpainting methods. digital image reconstruction and restoration, 04 2023.
- [24] James R. Lemen, Alan M. Title, David J. Akin, Paul F. Boerner, Catherine Chou, Jerry F. Drake, Dexter W. Duncan, Christopher G. Edwards, Frank M. Friedlaender, Gary F. Heyman, Neal E. Hurlburt, Noah L. Katz, Gary D. Kushner, Michael Levay, Russell W. Lindgren, Dnyanesh P. Mathur, Edward L. McFeaters, Sarah Mitchell, Roger A. Rehse, Carolus J. Schrijver, Larry A. Springer, Robert A. Stern, Theodore D. Tarbell, Jean-Pierre Wuelser, C. Jacob Wolfson, Carl Yanari, Jay A. Bookbinder, Peter N. Cheimets, David Caldwell, Edward E. Deluca, Richard Gates, Leon Golub, Sang Park, William A. Podgorski, Rock I. Bush, Philip H. Scherrer, Mark A. Gummin, Peter Smith, Gary Auker, Paul Jerram, Peter Pool, Regina Soufli, David L. Windt, Sarah Beardsley, Matthew Clapp, James Lang, and Nicholas Waltham. The atmospheric imaging assembly (aia) on the solar dynamics observatory (sdo). *Solar Physics*, 275(1):17–40, Jan 2012.
- [25] Dan Liu, Wei Song, Ganghua Lin, and Haimin Wang. Solar Filament Segmentation Based on Improved U-Nets. *Solar Physics*, 296(12):176, December 2021.
- [26] Sébastien Marcel and Yann Rodriguez. Torchvision the machine-vision package of torch. In *Proceedings of the 18th ACM International Conference on Multimedia*, MM '10, page 1485–1488, New York, NY, USA, 2010. Association for Computing Machinery.
- [27] Stuart Mumford, Nabil Freij, Steven Christe, Jack Ireland, Florian Mayer, V. Hughitt, Albert Shih, Daniel Ryan, Simon Liedtke, David Pérez-Suárez, Pritish Chakraborty, Vishnuarayan K, Andrew Inglis, Punyaslok Pattnaik, Brigitta Sipócz, Rishabh Sharma, Andrew Leonard, David Stansby, Russell Hewett, Alex Hamilton, Laura Hayes, Asish Panda, Matt Earnshaw, Nitin Choudhary, Ankit Kumar, Prateek Chanda, Md Haque, Michael Kirk, Michael Mueller, Sudarshan Konge, Rajul Srivastava, Yash Jain, Samuel Bennett, Ankit Baruah, Will Barnes, Michael Charlton, Shane Maloney, Nicky Chorley, Himanshu, Sanskar Modi, James Mason, Naman, Jose Ivan Campos Roza, Larry Manley, Agneet Chatterjee, John Evans, Michael Malocha, Monica Bobra, Sourav Ghosh, Airmansmith, Dominik Stańczak, Ruben De Visscher, Shresth Verma, Ankit Agrawal, Dumindu Buddhika, Swapnil Sharma, Jongyeob Park, Matt Bates, Dhruv Goel, Garrison Taylor, Goran Cetusic, Jacob, Mateo Inchaurrendieta, Sally Dacie, Sanjeev Dubey, Deepankar Sharma, Erik Bray, Jai Rideout, Serge Zahniy, Tomas Meszaros, Abhigyan Bose, André Chicrala, Ankit, Chloé Guennou, Daniel D’Avella, Daniel Williams, Jordan Ballew, Nick Murphy, Priyank Lodha, Thomas Robitaille, Yash Krishan, Andrew Hill, Arthur Eigenbrot, Benjamin Mampaey, Bernhard Wiedemann, Carlos Molina, Duygu Keşkek, Ishtyaq Habib, Joseph Letts, Juanjo Bazán, Quinn Arbolante, Reid Gomillion, Yash Kothari, Yash Sharma, Abigail Stevens, Adrian Price-Whelan, Ambar Mehrotra, Arseniy Kustov, Brandon Stone, Trung Dang, Emmanuel Arias, Fionnlagh Dover, Freek Verstringe, Gulshan Kumar, Harsh Mathur, Igor Babuschkin, Jaylen Wimbish, Juan Buitrago-Casas, Kalpesh Krishna, Kaustubh Hiware, Manas Mangaonkar, Matthew Mendero, Mickaël Schoentgen, Norbert Gyenge, Ole Streicher, Rajasekhar Mekala, Rishabh Mishra, Shashank Srikanth, Sarthak Jain, Tanmay Yadav, Tessa Wilkinson, Tiago Pereira, Yudhik Agrawal, Jamescalixto, Yasintoda, and Sophie Murray. SunPy: A Python package for Solar Physics. *The Journal of Open Source Software*, 5(46):1832, February 2020.
- [28] N. Otsu. A threshold selection method from gray-level histograms. *IEEE Transactions on Systems, Man, and Cybernetics*, 9(1):62–66, Jan 1979.
- [29] Sreejith Padinhatteeri, Paul A. Higgins, D. Shaun Bloomfield, and Peter T. Gallagher. Automatic Detection of Magnetic δ in Sunspot Groups. *Solar Physics*, 291(1):41–53, January 2016.

-
- [30] Adam Paszke, Sam Gross, Francisco Massa, Adam Lerer, James Bradbury, Gregory Chanan, Trevor Killeen, Zeming Lin, Natalia Gimelshein, Luca Antiga, Alban Desmaison, Andreas Kopf, Edward Yang, Zachary DeVito, Martin Raison, Alykhan Tejani, Sasank Chilamkurthy, Benoit Steiner, Lu Fang, Junjie Bai, and Soumith Chintala. Pytorch: An imperative style, high-performance deep learning library. In *Advances in Neural Information Processing Systems 32*, pages 8024–8035. Curran Associates, Inc., 2019.
- [31] W. Dean Pesnell, B. J. Thompson, and P. C. Chamberlin. The Solar Dynamics Observatory (SDO). *Solar Physics*, 275(1-2):3–15, January 2012.
- [32] Adrian M Price-Whelan, BM Sipőcz, HM Günther, PL Lim, SM Crawford, S Conseil, DL Shupe, MW Craig, N Dencheva, A Ginsburg, et al. The astropy project: Building an open-science project and status of the v2. 0 core package. *The Astronomical Journal*, 156(3):123, 2018.
- [33] Ming Qu, Frank Y. Shih, Ju Jing, and Haimin Wang. Automatic Solar Filament Detection Using Image Processing Techniques. *Solar Physics*, 228(1-2):119–135, May 2005.
- [34] Sarkar et al. Test and Calibration of the Solar Ultraviolet Imaging Telescope (SUIT). *Solar Physics*, in prepatation, 2025.
- [35] Michael Schuh and Rafal Angryk. Massive labeled solar image data benchmarks for automated feature recognition. 10 2014.
- [36] Michael A Schuh, Rafal A Angryk, Karthik Ganesan Pillai, Juan M Banda, and Petrus C Martens. A large-scale solar image dataset with labeled event regions. In *2013 IEEE International Conference on Image Processing*, pages 4349–4353. IEEE, 2013.
- [37] Juan Terven, Diana-Margarita Córdova-Esparza, and Julio-Alejandro Romero-González. A comprehensive review of yolo architectures in computer vision: From yolov1 to yolov8 and yolo-nas. *Machine Learning and Knowledge Extraction*, 5(4):1680–1716, November 2023.
- [38] Durgesh Tripathi, Dibyendu Chakrabarty, A. Nandi, B. Prasad, Anamparambu Ramaprakash, Nigar Shaji, K. Sankarasubramanian, R. Thampi, and Vipin Yadav. The aditya-l1 mission of isro. *Proceedings of the International Astronomical Union*, 18:17–27, 09 2023.
- [39] Durgesh Tripathi, A. N. Ramaprakash, Aafaque Khan, Avyarthana Ghosh, Subhamoy Chatterjee, Dipankar Banerjee, Pravin Chordia, Achim Gandorfer, Natalie Krivova, Dibyendu Nandy, Chaitanya Rajarshi, and Sami K. Solanki. The solar ultraviolet imaging telescope on-board aditya-l1. *Current Science*, 113(04):616, August 2017.
- [40] Stéfan van der Walt, Johannes L. Schönberger, Juan Nunez-Iglesias, François Boulogne, Joshua D. Warner, Neil Yager, Emmanuelle Gouillart, Tony Yu, and the scikit-image contributors. scikit-image: image processing in Python. *PeerJ*, 2:e453, 6 2014.
- [41] Madhan Veeramani and M. S. Sudhakar. Automatic detection of sunspots on solar continuum HMI images blending local-global threshold. *New Astronomy*, 105:102089, January 2024.
- [42] Pauli Virtanen, Ralf Gommers, Travis E. Oliphant, Matt Haberland, Tyler Reddy, David Cournapeau, Evgeni Burovski, Pearu Peterson, Warren Weckesser, Jonathan Bright, Stéfan J. van der Walt, Matthew Brett, Joshua Wilson, K. Jarrod Millman, Nikolay Mayorov, Andrew R. J. Nelson, Eric Jones, Robert Kern, Eric Larson, C J Carey, İlhan Polat, Yu Feng, Eric W. Moore, Jake VanderPlas, Denis Laxalde, Josef Perktold, Robert Cimrman, Ian Henriksen, E. A. Quintero, Charles R. Harris, Anne M. Archibald, Antônio H. Ribeiro, Fabian Pedregosa, Paul van Mulbregt, and SciPy 1.0 Contributors. SciPy 1.0: Fundamental Algorithms for Scientific Computing in Python. *Nature Methods*, 17:261–272, 2020.

- [43] S. Šimberová, M. Karlický, and T. Suk. Statistical Moments of Active-Region Images During Solar Flares. *Solar Physics*, 289(1):193–209, January 2014.
- [44] Stéfan van der Walt, S. Chris Colbert, and Gaël Varoquaux. The numpy array: A structure for efficient numerical computation. *Computing in Science & Engineering*, 13(2):22–30, 2011.
- [45] Chien-Yao Wang, I-Hau Yeh, and Hong-Yuan Mark Liao. Yolov9: Learning what you want to learn using programmable gradient information, 2024.
- [46] Michael Waskom, Olga Botvinnik, Drew O’Kane, Paul Hobson, Saulius Lukauskas, David C Gemperline, Tom Augspurger, Yaroslav Halchenko, John B. Cole, Jordi Warmenhoven, Julian de Rutter, Cameron Pye, Stephan Hoyer, Jake Vanderplas, Santi Villalba, Gero Kunter, Eric Quintero, Pete Bachant, Marcel Martin, Kyle Meyer, Alistair Miles, Yoav Ram, Tal Yarkoni, Mike Lee Williams, Constantine Evans, Clark Fitzgerald, Brian, Chris Fonesbeck, Antony Lee, and Adel Qalieh. mwaskom/seaborn: v0.8.1 (september 2017), September 2017.
- [47] Y. Yuan, F. Y. Shih, J. Jing, H. Wang, and J. Chae. Automatic Solar Filament Segmentation and Characterization. *Solar Physics*, 272(1):101, August 2011.
- [48] Cui Zhao, GangHua Lin, YuanYong Deng, and Xiao Yang. Automatic Recognition of Sunspots in HSOS Full-Disk Solar Images. *Publications of the Astronomical Society of Australia*, 33:e018, May 2016.